



**HAL**  
open science

## **XMapTools: A MATLAB©-based program for electron microprobe X-ray image processing and geothermobarometry**

Pierre Lanari, Olivier Vidal, Vincent de Andrade, Benoît Dubacq, Eric Lewin, Eugene G. Grosch, Stéphane Schwartz

### ► To cite this version:

Pierre Lanari, Olivier Vidal, Vincent de Andrade, Benoît Dubacq, Eric Lewin, et al.. XMapTools: A MATLAB©-based program for electron microprobe X-ray image processing and geothermobarometry. *Computers & Geosciences*, 2014, 62, pp.227-240. 10.1016/j.cageo.2013.08.010 . hal-00927675

**HAL Id: hal-00927675**

**<https://hal.science/hal-00927675v1>**

Submitted on 21 Jan 2014

**HAL** is a multi-disciplinary open access archive for the deposit and dissemination of scientific research documents, whether they are published or not. The documents may come from teaching and research institutions in France or abroad, or from public or private research centers.

L'archive ouverte pluridisciplinaire **HAL**, est destinée au dépôt et à la diffusion de documents scientifiques de niveau recherche, publiés ou non, émanant des établissements d'enseignement et de recherche français ou étrangers, des laboratoires publics ou privés.

1 **XMapTools: a MATLAB©-based program for**  
2 **electron microprobe X-ray image processing and**  
3 **geothermobarometry**

4

5 *Pierre Lanari<sup>a,b,\*</sup>, Olivier Vidal<sup>b</sup>, Vincent De Andrade<sup>c</sup>, Benoît Dubacq<sup>d,e,f</sup>, Eric*  
6 *Lewin<sup>b</sup>, Eugene G. Grosch<sup>g</sup> and Stéphane Schwartz<sup>b</sup>*

7

8 <sup>a</sup> Institute of Geology, University of Bern, Baltzstrasse 1+3, CH-3012 Bern, Switzerland.

9 <sup>b</sup> ISTERre, Université de Grenoble I, CNRS, 1381 rue de la Piscine. 38041 Grenoble, France.

10 <sup>c</sup> NSLS II, Brookhaven National Laboratory, SRX beamline, Bldg 817 Renaissance Road, Upton, New  
11 York 11973, USA.

12 <sup>d</sup> Department of Earth Sciences, University of Cambridge, Downing Street, Cambridge CB2 3EQ, UK

13 <sup>e</sup> UPMC Univ. Paris 06, ISTEP, UMR 7193; F-75005 Paris, France

14 <sup>f</sup> CNRS, ISTEP, UMR 7193; F-75005 Paris, France.

15 <sup>g</sup> Department of Earth Science and Centre for Geobiology, University of Bergen, Allegaten 41, N-  
16 5007, Bergen, Norway.

17

18 \*Corresponding author. Fax +41 031 631 48 43.

19 E-mail address: pierre.lanari@geo.unibe.ch (P. Lanari)

20

21

22

23 **Computers & Geosciences, 62 (2014) 227-240**

24

25

26 **Abstract**

27

28 *XMapTools* is a *MATLAB*<sup>®</sup>-based graphical user interface program for electron  
29 microprobe X-ray image processing, which can be used to estimate the pressure-  
30 temperature conditions of crystallization of minerals in metamorphic rocks. This  
31 program (available online at <http://www.xmaptools.com>) provides a method to  
32 standardize raw electron microprobe data and includes functions to calculate the oxide  
33 weight percent compositions for various minerals. A set of external functions is  
34 provided to calculate structural formulae from the standardized analyses as well as to  
35 estimate pressure-temperature conditions of crystallization, using empirical and semi-  
36 empirical thermobarometers from the literature. Two graphical user interface  
37 modules, *Chem2D* and *Triplot3D*, are used to plot mineral compositions into binary  
38 and ternary diagrams. As an example, the software is used to study a high-pressure  
39 Himalayan eclogite sample from the Stak massif in Pakistan. The high-pressure  
40 paragenesis consisting of omphacite and garnet has been retrogressed to a  
41 symplectitic assemblage of amphibole, plagioclase and clinopyroxene. Mineral  
42 compositions corresponding to ~165 000 analyses yield estimates for the eclogitic  
43 pressure-temperature retrograde path from 25 kbar to 9 kbar. Corresponding pressure-  
44 temperature maps were plotted and used to interpret the link between the equilibrium  
45 conditions of crystallization and the symplectitic microstructures. This example  
46 illustrates the usefulness of *XMapTools* for studying variations of the chemical  
47 composition of minerals and for retrieving information on metamorphic conditions on  
48 a microscale, towards computation of continuous pressure-temperature-and relative  
49 time path in zoned metamorphic minerals not affected by post-crystallization  
50 diffusion.

51

52 **Keywords:** *XMapTools* program; X-ray chemical imaging; quantitative micro-  
53 mapping; *PT*-maps

54

55

## 56 **1. Introduction**

57 Our understanding of the geodynamics and processes in orogens, subduction zones  
58 and the lower crust relies on estimations of the pressure-temperature (*P-T*) conditions  
59 of crystallization of mineral assemblages. Deriving reliable pressure and temperature  
60 information from a rock is critical to our knowledge of the thermal structure of the  
61 crust, whose variations can be recorded through time within individual samples via  
62 consecutive partial re-equilibration events. Thermobarometric tools such as multi-  
63 equilibrium thermobarometry (e.g. Berman, 1991), pseudosections (e.g. Holland and  
64 Powell, 1998; 2011) and empirical thermometers (e.g. Cathelineau and Nieva, 1985)  
65 provide these estimates from the nature and composition of minerals, even for high-  
66 variance assemblages (Vidal and Parra, 2000). To shed light on the recrystallization  
67 history of metamorphic rocks, chemical compositions of the minerals are required.  
68 This is commonly achieved using point mode analyses obtained with an electron  
69 probe microanalyser (EPMA). The use of X-ray images allows to identify the  
70 relationships between microstructures, variations of composition and variations of *P-T*  
71 conditions of crystallization (e.g. Vidal et al., 2006). Since the first X-ray “dot maps”  
72 compositional image (Cosslett and Duncumb 1956), this technique has been  
73 developed (see Friel and Lyman 2006 for a review) using both energy-dispersive and  
74 wavelength dispersive X-ray spectrometers (EDS and WDS). For instance, previous  
75 work has used X-ray images for classification and modal analysis (Launeau et al.,

76 1994; Bonnet, 1998; Cossio et al., 2002; Prêt et al., 2010) and to reconstruct *P-T* paths  
77 (Kohn and Spear, 2000; De Andrade et al., 2006; Muñoz et al., 2006; Vidal et al.,  
78 2006; Yamato et al., 2007; Ganne et al., 2012; Fiannacca et al., 2012; Lanari et al.,  
79 2012; Plunder et al., 2012; Pourteau et al., 2013; Lanari et al., 2013). Quantitative  
80 electron microprobe analyses require an analytical standardization of the number of  
81 collected photons (X-ray intensity). The acquisition time for standardized point  
82 analysis for eight major elements (e.g. Si, Al, Mn, Mg, Fe, Na, Ca, K) under classical  
83 conditions (typically 10nA, 15keV, 40s) averages around two minutes. This approach  
84 is therefore difficult to apply to chemical mapping, where samples are typically  
85 heterogeneous on a ~10µm scale and maps typically contain about 150 000 pixels,  
86 that would correspond to ~200 days of measurements. X-ray maps for quantitative  
87 mapping can be obtained within a reasonable time frame by using a higher current  
88 intensity and a lower counting time (100nA, 15 KeV, 100-300ms, see De Andrade et  
89 al., 2006). In order to transform the X-ray intensities into calibrated weight  
90 percentages, Clarke et al. (2001) used a Bence-Albee approach (Bence and Albee,  
91 1968), which has been later implemented in the program XRMMapAnal (Tinkham and  
92 Ghent, 2005). However, the precision of this standardization procedure is subject to  
93 caution, because it can result in unreliable compositions for some geologically  
94 important phases (e.g. quartz, muscovite, plagioclase and garnet, compositions listed  
95 in the table 3 of Tinkham and Ghent, 2005). De Andrade et al. (2006) showed that  
96 standardization of X-ray intensities using point analyses as internal standards  
97 (Castaing, 1951) provides more reliable results.

98 In the present contribution, we present a *MATLAB*<sup>®</sup>-based Graphical User Interface  
99 (GUI) program named *XMapTools* that can be used to: (1) classify mineral phases in  
100 the sample, (2) convert X-ray intensities into calibrated weight percentages using

101 Castaing's approach, (3) calculate the structural formulae of the identified minerals,  
102 (4) plot minerals compositions using various chemical diagrams, and (5) calculate  $P$ - $T$   
103 conditions of equilibration using various empirical and semi-empirical  
104 thermobarometers. An example of application of the program to a retrogressed  
105 eclogite is presented below.

106

## 107 **2. Description of the program**

108 The *XMapTools* program (available at <http://www.xmaptools.com>) can be run with a  
109 *MATLAB*<sup>®</sup> version 7.5 release R2007b or later. It uses a graphical interface named  
110 *XMapTools.fig* (Fig. 1) built using the *MATLAB*<sup>®</sup> Graphical User Interface  
111 Development Environment (GUIDE) tool. Each of the GUI components dragged with  
112 the GUIDE is associated with a callback function in the program file *XMapTools.p*,  
113 corresponding to a content-obscured version (encrypted executable).

114 The program is structured into three parts: *Xray*, *Quanti* and *Results* (Fig. 2)  
115 corresponding to three different steps of the mapping process. The first step (*Xray*  
116 column in Fig. 2), starts by loading the map. From statistical analysis of their  
117 composition, pixels are grouped within mineral phases and possibly fractures or  
118 voids, and corresponding masks are created. The user then identifies the nature of the  
119 various groups. This step ends with the standardization stage. In the second step,  
120 (*Quanti* column in Fig. 2), standardized maps are turned into maps of structural  
121 formulae and into  $P$ - $T$  maps. The last step (*Results* column in Fig. 2), allows the user  
122 to produce binary and ternary chemical diagrams with the *Chem2D* and *TriPlot3D*  
123 modules. All the functions used in these different stages are detailed below.

124

### 125 **2.1 Raw data treatment (Xray)**

126 Two types of datasets can be uploaded into *XMapTools*, namely the raw X-ray data in  
127 photon counts per pixel (matrixes corresponding to the number of collected photons  
128 per analyzed element per pixel) and the point analyses used as internal standards.

129 With both *Cameca*<sup>®</sup> and *Jeol*<sup>®</sup> EPMA, the raw data of chemical maps can be exported  
130 in *ASCII* format text files such as *\*.txt* file. Typically, one file is created for each  
131 measured element, and contains header lines reporting information about analytical  
132 conditions and coordinates of the selected area, followed by a matrix of X-ray  
133 intensity data (see Appendix 1). After removal of the header lines by the user, the  
134 loading function of *XMapTools* reads the input files and creates X-ray intensity  
135 images. This function includes dead-time correction, where the time interval after the  
136 arrival of a pulse during which the spectrometer is unresponsive to further pulses  
137 (Reed 2005) is accounted for, and transforms the measured counting rates into true  
138 rates.

139 Point analyses, their coordinates and the map coordinates are the other required inputs  
140 to the standardization step. Usually, the point analyses are made along different  
141 transects at high angles to (mineral grain boundaries includes 'each other') mineral  
142 grain boundaries to capture the total extent of the minerals heterogeneity. Experience  
143 has shown that a minimum of 20 point analyses encompassing most of the chemical  
144 heterogeneity of each mineral phases in the selected area of the sample is necessary to  
145 reach optimum precision. The standard loading function reads a series of point  
146 analyses. The locations of the point analyses must be carefully reported from stage  
147 coordinates corrected for mechanical backlash and are then projected on the map with  
148 the EMPA map coordinate system. The user can compare the X-ray intensities along  
149 the profiles measured by point analyses to those of the map, which is useful to detect  
150 problems of location of profiles on the map, for example due to drifting of the sample

151 stage during analysis or to a projection problem. The point analyses showing outlying  
152 or unwanted compositions such as mixtures of fine minerals, inclusions, or grain  
153 boundaries must be deleted before the standardization.

154

### 155 **2.1.1 Classification: mask creating function**

156 This function creates masks corresponding to entities identified in the map (e.g.  
157 mineral, mineral boundaries, fractures), where each mask is a matrix of logical  
158 numbers indexed on the coordinates of the composition map: the value of 1 is  
159 attributed to the pixels belonging to a given mineral phase, and 0 to the other pixels.

160 This function allocates each individual pixel to one of the minerals phases. The mask  
161 creating function uses the statistical analysis method K-means clustering to distribute  
162 the pixels into groups of similar compositions. K-means identifies clusters and  
163 allocates pixels to these clusters by minimization of the distance in compositional  
164 space between the pixels and the gravity centre of each cluster (Saporta 1990).

165 The user selects one pixel of each phase on the chemical map as needed by the mask  
166 creating function for initial guess. The compositions of these pixels are used as  
167 starting cluster centroids. In an iterative loop, each pixel is assigned to the nearest  
168 cluster and the centroids are recalculated until the sum of point-to-centroid  
169 distances over all clusters is minimized (Seber, 1984; Spath, 1985). Two approaches  
170 are available in *XMapTools*: the ‘normalized’ and the ‘classical’ approaches. Both of  
171 them use a K-means clustering approach, but with different X-ray intensities inputs.  
172 In the ‘normalized’ function, X-ray intensities of each element are normalized to their  
173 mean values, with the result that all elements have the same weight and only the  
174 variances are compared. In contrast, the X-ray intensities of each element in the  
175 ‘classical’ method depend on the absolute concentration in each element. This



176 'classical' method is therefore more appropriate for elements present in high  
177 concentration. Different masks may be derived using both methods, depending on the  
178 magnitude of the differences between the compositions of the phases. An example is  
179 shown in section 3.2. Other approaches for the classification of different mineral  
180 phases can be found in the PetroMod program (Cossio et al., 2002). Here the K-means  
181 algorithm was chosen for its straightforwardness and efficiency.

182

### 183 **2.1.2 Standardization function**

184 The analytical standardization consists in converting the measured X-ray intensities  
185 into oxide weight percent concentrations using standards (Reed, 2005). The  
186 standardization function performs this transformation for each mask where  
187 quantitative information is available from point analysis or using user-defined  
188 concentrations. The standardization of pixels requires calibration curves describing  
189 how X-ray intensities change with concentration (Castaing, 1951). One calibration  
190 curve is calculated for each element in each phase from the intensity versus  
191 concentration relations constrained with point analyses. The calibration curves for Si  
192 in the different phases of the studied sample are shown in Figure 3. For each mineral,  
193 the calibration curve is a straight line between the origin (0 intensity and  
194 concentration) and the central point of the cluster of the point analyses.

195 The standardization can be performed using one of the three methods available in  
196 *XMapTools*. The first method 'Auto (median approach)' is fully automatic, and the  
197 cluster centroids are the median values separating the higher half from the lower half  
198 of the data. The 'Manual' approach allows the user to define the center of the clusters  
199 and therefore the calibration curve. The last method 'Manual (homogeneous phase)' is  
200 adapted to minerals assumed to be homogeneous such as might be the case for quartz.

201 The calibration curve is then defined as the mean value of X-ray intensity for the  
202 selected mineral and the user enters the corresponding concentration, e.g. 100% for  
203 SiO<sub>2</sub> in the case of quartz.

204

## 205 **2.2 Calculations from quantified data (Quanti)**

206 Once the masks have been defined and element concentrations have been estimated,  
207 structural formulae may be calculated and equilibrium conditions derived using  
208 external functions (see below). Users can add new thermobarometry or structural  
209 formula functions. The file ‘List-thermometers.txt’ lists all information about these  
210 external functions (i.e. category, name, input and output variables) that are stored into  
211 the folder ‘Functions’. All these functions are *MATLAB*<sup>®</sup> script m-files that can be  
212 read and edited.

213

### 214 **2.2.1 Structural formulae functions**

215 Several structural formulae and atom site allocations models from the literature are  
216 implemented in *XMapTools* (Table 1). A general function is also available to calculate  
217 a structural formula normalized to a given number of oxygen atoms. This additional  
218 function is used to compute the number of moles of elements per formula unit (p.f.u.)  
219 for each pixel assuming that the total sums up to 100%.

220

### 221 **2.2.2 Thermobarometry functions**

222 *XMapTools* includes a large selection of thermobarometry functions based on  
223 empirical and semi-empirical calibrations. These methods are distributed into two  
224 groups: exchange reactions for thermometry (Table 2) and thermobarometer functions  
225 (Table 3).

226 In exchange reactions, cations such as  $\text{Fe}^{2+}$  and  $\text{Mg}^{2+}$  are swapped between two  
227 minerals (e.g. Spear, 1995).  $P$ - $T$  conditions of equilibrium may be derived from the  
228 cations partition between the two phases (e.g., Ravna, 2000a for garnet-  
229 clinopyroxene). *XMapTools* generates an image with the oxide weight percent  
230 compositions of the two minerals and allows the user to select pairs of pixels (spot  
231 mode) or pairs of groups of pixels (area mode).

232 In the spot mode, the selected compositions are used to estimate the equilibrium  
233 conditions. In the area mode, all the possible pairs of pixels are used to calculate an  
234 average equilibrium condition with associated uncertainty. This mode allows to  
235 propagate the effect of composition variation in any phase through the whole  
236 thermobarometer calculation.

237 For exchange reactions,  $T$  is usually estimated for a given pressure. If the minerals  
238 exhibit metamorphic zoning preserving paleo-equilibrium conditions, and if the  
239 zoning pattern is not due to post-crystallization diffusion, the variations of  $T$   
240 conditions can be investigated using exchange reactions. A set of mineral pairs  
241 selected between the core and the rim of two minerals provides a trend for the  
242 evolution of the temperature conditions. This approach is essentially the same as  
243 commonly used with point analyses.

244 The thermobarometry functions provide information on the  $T$  and/or  $P$  of mineral  
245 crystallization for each pixel of the map, which can be turned into  $P$ ,  $T$ , or  $P$  and  $T$   
246 maps. Both  $P$  and  $T$  conditions are derived from only one mineral composition (one  
247 pixel) with fixed variables such as other mineral composition, or  $P$  or  $T$ . Methods are  
248 listed in Table 3 in three groups: (1) thermometers, (2) barometers, and (3)  
249 thermobarometers where  $P$ - $T$  conditions are derived from at least two reactions (one  
250  $T$ -dependent and one  $P$ -dependent) within a given mineral assemblage. This is done

251 using groups of pixel compositions and assuming equilibrium between the groups.  
252 The use of thermobarometry functions should be restrained to cases where the  
253 relevant saturating assemblages are present in the studied sample. The functions  
254 implemented in XMapTools do not check the presence of such assemblages because  
255 some minerals may be outside the mapped area. This is then the responsibility of the  
256 user to decide whether the functions can be applied to the studied sample.

257

### 258 **2.3 Chemical plots**

259 The mineral compositions or end-member proportions can be plotted as maps or into  
260 chemical diagrams such as binary diagrams (Fig. 4a) using the *Chem2D* module, or  
261 ternary diagrams (Fig. 5a) using the *Triplot3D* module. Both modules have a  
262 graphical interface in which the user can select the plotted variables and manage the  
263 diagram axes. A density plot function is also available to contour the analyzed  
264 variables for density, which is useful when a large number of points is plotted as is the  
265 case when working with maps (see examples in Fig. 4b and 5b). This function  
266 displays a density map using the mineral composition data and grid spacing defined  
267 by the user for density counting. The unit of the output of the density map is a number  
268 of analyses per surface unit of the grid on the graph, which has the dimension of the  $x$   
269 axis multiplied to the  $y$  axis.

270 Two selection functions, namely ‘identify pixels’ and ‘multi-groups’, may be used to  
271 select ranges of composition (rectangles) in the diagrams, as well as to identify the  
272 selected pixels on the corresponding map (Fig. 4c and Fig. 5c) and to calculate modal  
273 abundances.

274 Several functions may be used to create masks from user-defined chemical groups  
275 within a phase. These masks are either built from manual selections (with the tools

276 “identify pixel” and “multi-groups”) or automatically using a K-means clustering  
277 approach. The mask variable can be exported into ASCII format (\*.txt file) and used  
278 in the *Quanti* stage to export the average oxide composition corresponding to a  
279 selection of pixels.

280

## 281 **2.4 Other functions**

282 All the results can be saved and previously saved projects can be loaded at any time  
283 using the functions ‘save’, ‘save as’ and ‘load’. The save functions store the data in a  
284 MATLAB© formatted binary file MAT-file (with .mat extension).

285 Functions in the ‘figure’ window are dedicated to the management of the color bar  
286 such as setting the minimum and maximum values, the auto and reset buttons, and the  
287 phase separator button (PhaseSep in Fig. 1). The user can also export the main figure  
288 in usual image formats.

289 Functions in the ‘sampling’ window are used to select a subset of the data into the  
290 main displayed image. These functions are available for any image (X-ray raw  
291 measurement, map of oxide compositions, structural formulae, equilibrium conditions  
292 maps). The selected data may be individual pixels, arrays or areas of pixels. This tool  
293 can be used for example to draw the composition variations of a mineral grain along a  
294 transect.

295

## 296 **3. Tests and evaluation**

297 Generating structural formulae and *P-T* maps from microprobe analysis is of interest  
298 for petrology and geodynamics studies. In this section, we present an example of the  
299 use of *XMapTools* on a metamorphic rock sample. Compositional maps were acquired  
300 on an eclogite sample from the Stak area, a high pressure (HP) continental massifs in

301 NW Himalaya (Guillot et al., 2008; Lanari et al., 2013). This sample contains a well-  
302 preserved eclogitic assemblage consisting of garnet and omphacite, which formed  
303 during continental subduction. Omphacite was subsequently retrogressed to a Na-  
304 poorer clinopyroxene + plagioclase + amphibole symplectite. The final metamorphic  
305 event is recorded in the sample as a foliation comprising large crystals of amphibole  
306 developed as a result of deformation and syntectonic hydration under mid-upper  
307 crustal conditions (Lanari et al., 2013).

308

### 309 **3.1 Data acquisition**

310 An area of 0.348 mm<sup>2</sup> (520µm × 670µm) located in a symplectite zone and containing  
311 garnet, clinopyroxene, amphibole, plagioclase, Ti- and Fe-oxides was mapped at the  
312 Institute of Earth and Environmental Science, University of Potsdam, using a JEOL  
313 JXA-8200 EMPA. Mapping conditions were 15 keV accelerating voltage and 100 nA  
314 beam current, beam diameter smaller than 1 µm, 200 ms dwell time and 1 µm step  
315 size (i.e. pixel size). X-ray intensities for Si, Ti, Al, Fe, Mg, Mn, Ca, Na and K were  
316 measured in two passes.

317

### 318 **3.2 Classification**

319 An image of the mineral phases created using the ‘mask creating function’ (see §2.1)  
320 is shown in Figure 6a. The two methods for the mask creating function (classical and  
321 normalized) were tested and lead to similar estimates of the mineral modal  
322 proportions except for garnet (Table. 4). The difference for garnet is due to the  
323 erroneous allocation of the contour pixels around amphibole to the garnet mask when  
324 using the classical approach. This artefact may be corrected by creating an additional  
325 mask corresponding to the borders of the mineral or by using the normalized method.

326 Additional differences between the ‘normalized’ and ‘classical’ approaches are shown  
327 in Figure 6b for a part of the map (dashed square in Fig. 6a). For instance, zone 1 in  
328 Fig. 6b shows that omphacite is identified in the core of clinopyroxene using the  
329 ‘normalized’ method only. This is due to the normalization procedure and originates  
330 from the small chemical differences between omphacite and clinopyroxene in their  
331 Na- and Mg-contents. These differences are not detected with the ‘classical’ method,  
332 which allocates more pixels to the clinopyroxene mask. The other examples (2 and 3  
333 in Fig. 6) show that in some cases, the opposite effect is observed when variations  
334 occur in only one highly concentrated element, keeping effects of the variations in  
335 low-concentrated elements to a minimum. From this, we conclude that the two  
336 methods should be tested and we recommend to check the difference between the two  
337 results and to compute different mask-files with different number of phases (including  
338 the fractures and/or mineral boundaries).

339

#### 340 **3.4 Test of the standardization**

341 Analytical standardization of the X-ray images was performed using the  
342 ‘standardization function’ (see §4.1) with the ‘Auto (median approach)’ method.  
343 Calibration curves (see §3.1 and graphical representation in Fig. 3) were calculated  
344 for clinopyroxene, garnet, amphibole and plagioclase.

345 The quality and accuracy of the standardization can be investigated using the function  
346 ‘Test of standardization’. This function plots the composition difference between  
347 point analyses and the standardized composition on the same location on the maps. As  
348 an example, the results for the standardization of garnet are reported in Fig. 8, which  
349 shows that the pixel compositions derived from the standardized maps are in good  
350 agreement, within analytical uncertainties, with the corresponding point analyses for

351 elements showing homogeneous compositions such as SiO<sub>2</sub>, Al<sub>2</sub>O<sub>3</sub>, FeO (Fig. 8a, 8b  
352 and 8c) and heterogeneous compositions due to zoning such as CaO, MgO and MnO  
353 (Fig. 8d, 8e and 8f). In contrast, the point analyses of low concentration elements  
354 TiO<sub>2</sub> and K<sub>2</sub>O show trends not recorded in the standardized maps (Fig. 8g and 8h),  
355 indicating that the concentrations of TiO<sub>2</sub> and K<sub>2</sub>O mapped in garnet are not reliable,  
356 because they are close to the detection limits for the used mapping analytical  
357 conditions.

358

### 359 **3.5 Structural formulae and chemical study**

360 Clinopyroxene structural formulae were calculated on a 6 oxygen-basis by  
361 distributing elements on tetrahedral (T1) and octahedral (M1, M2) sites. End-  
362 members proportions of jadeite, diopside, hedenbergite, acmite and Ca-tschermak  
363 (Table 1) were estimated according to the atom site allocation model of Spear (1995)  
364 and Warren and Waters (2006). The amphiboles structural formulae were calculated  
365 on a 23 oxygen-basis and elements were distributed on tetrahedral (T1, T2),  
366 octahedral (M2, M13, M4), and 10 to 12-fold coordinated (A) sites. End-members  
367 proportions of glaucophane, tremolite, tschermakite, pargasite, cumingtonite (Table 1)  
368 were calculated according to the atom site allocation model of Dale et al. (2000;  
369 2005). Structural formulae for garnet and plagioclase were respectively calculated on  
370 a 12 and 8 oxygen-basis following classical atom-site allocation models (Table 1).  
371 Structural formulae maps highlight the relationship between atom-site composition  
372 and microstructures. The two chemical modules *Chem2D* and *Triplot3D* were used to  
373 investigate the variations of clinopyroxene structural formulae (i.e. varying end-  
374 member proportions). In Figure 4a, Na-rich clinopyroxene compositions were  
375 selected (red dots) using the ‘identify pixel’ tool (§2.3) in the Na vs. Mg diagram. The



376 pixels belonging to the selected composition range are plotted in red on the map (Fig.  
377 4c). These Na-rich clinopyroxene compositions are omphacitic and make up to ~25%  
378 of the total clinopyroxene pixels. Then, clinopyroxene compositions were divided into  
379 three groups using the ‘multi-groups’ tool within the jadeite-diopside-hedenbergite  
380 ternary diagram (groups 1, 2 and 3 in Fig. 5a). The pixels belonging to the three  
381 composition ranges are plotted on the map with corresponding colors (Fig. 5c). The  
382 clinopyroxene compositions into the symplectite have lower Na contents,  
383 corresponding to lower jadeite contents. Clinopyroxene-amphibole-plagioclase  
384 symplectites are known to nucleate on grain boundaries between two omphacite  
385 grains and to grow into the grain on one side, when the rock is sufficiently out of  
386 equilibrium to nucleate the product (Joanny et al., 1991; Waters, 2002, 2003). In the  
387 mapped area (Fig. 7), Na-rich clinopyroxene previously identified as omphacite  
388 shows high Na contents (up to 0.4 p.f.u, zone 1 in Fig. 7). This primary omphacite  
389 (width > 100 $\mu$ m) is destabilized into a first symplectite containing Na-poorer  
390 clinopyroxene, plagioclase and amphibole. Clinopyroxene in this first symplectite  
391 (zone 2 in Fig. 7) crystallizes as broad lamellae (30-40 $\mu$ m width) preserving the  
392 original shape of omphacite, but with a lower Na-content (0.35 to 0.28 p.f.u.) than the  
393 original omphacite grains. A second symplectite with the same minerals is observed  
394 in zone 3 of figure 7, which shows smaller-size clinopyroxene lamellae (10-20 $\mu$ m  
395 width) and Na-content (0.28 to 0.18 p.f.u.). Clinopyroxene lamellae are even smaller  
396 in the last symplectite (width < 10 $\mu$ m) and also have lower Na-content (<15 p.f.u.).

397

### 398 **3.6 Precision and resolution**

399 In the previous section, maps of structural formulae highlight variations in the  
400 clinopyroxene composition according to the symplectite microstructures. Na-content

401 in clinopyroxene decreases with decreasing size of the symplectite (i.e. with time).  
402 The clinopyroxene solid solution includes jadeite while diopside hedenbergite and Ca-  
403 tschermak are calcic end-members. As the multiplicity of the M2 site is one and  
404  $X_{Fe^{3+}} = 0$  (corresponding to  $X_{acmite} = 0$ ), the jadeite proportion is equal to the Na-  
405 content in clinopyroxene. Estimating the uncertainties associated with the  
406 compositional values of the structural formulae is needed before discussing the  
407 implications linked to the chemical zoning.  
408 The precision of the electron microprobe measurement with our experimental protocol  
409 can be estimated using a Poisson law (De Andrade et al., 2006):

$$410 \quad p = \frac{2}{\sqrt{n}} \quad (1)$$

411 with  $p$  the precision (in % at  $2\sigma$ ), and  $n$  the number of recorded counts. The mean  
412 intensities and precision measurements for each element (Si, Ti, Al, Fe, Mg, Ca, Na,  
413 K) of clinopyroxene pixels are listed in Table 4. The precision measurements range  
414 from 1.8% for Si to 20% for Ti. Uncertainties in the structural formula originating  
415 from analytical errors were estimated using a Monte Carlo simulation where a total of  
416 100 000 random clinopyroxene compositions were computed with a normal  
417 distribution around the mean intensity compositions (Table 4) within  $2\sigma$  of the  
418 measured precisions. The standardization procedure was carried out for all the  
419 compositions using the calibration curves estimated above. The average oxide  
420 concentrations structural formulae and the associated standard deviations are listed in  
421 Table 4. The average Na-content is estimated at  $0.28 \pm 0.03$  p.f.u., which indicates  
422 that the compositional variations identified above (ranging from 0.41 to 0.13) are  
423 significant. It is emphasized that the uncertainties reported here are valid for the  
424 present EPMA settings and range of clinopyroxene composition, and can be decreased  
425 by increasing the dwell time.

426

### 427 **3.7 Combined *P* and *T* functions: *P-T* maps of Cpx**

428 *P-T* maps were built using combined *P* and *T* functions available in *XMapTools*  
429 (description in §4.2 and list in Table 2). At the thin section scale, two assemblages  
430 involving clinopyroxene are in equilibrium: the HP assemblage made of garnet,  
431 omphacite and phengite (as inclusions in garnet, not present in the mapped area) and  
432 the retrogressed assemblage represented by the clinopyroxene-plagioclase-amphibole  
433 symplectite. These two parageneses were treated separately.

434 For the HP assemblage, *P-T* conditions for clinopyroxene pixels were estimated using  
435 the *XMapTools* function ‘Cpx-P-T Rav (Omp-Gar-Phg)’. *P* was estimated using the  
436 garnet, omphacite and phengite geobarometer of Waters and Martin (1993) and  
437 Waters (1996). *T* was estimated using the garnet and omphacite geothermometer of  
438 Ravna (2000a). The function estimates first  $T_1$  at a given *P* ( $P_{\text{input}}$ ), and recalculates  
439  $T_{n+1}$  and  $P_{n+1}$  until convergence (respectively 5°C and 0.1 kbar) between  $T_n$  and  $T_{n+1}$   
440 and  $P_n$  and  $P_{n+1}$ . As the compositions of garnet show a slight zoning (Alm<sub>48</sub> Prp<sub>32-33</sub>  
441 Grs<sub>17-19</sub> Sps<sub>1</sub>), two average garnet compositions were defined, one for the core and  
442 one for the rim (Lanari et al., 2013). In both groups, garnet compositions are  
443 homogeneous within errors. Each pixel of omphacite was assumed in equilibrium  
444 with one garnet average composition (core-core, rim-rim). Then, *P-T* estimates were  
445 calculated for all omphacite compositions.

446 For the symplectite, *T* was first estimated using the edenite-richterite calibration  
447 (Holland and Blundy, 1994) with the composition of amphibole pixels for a fixed  
448 composition of plagioclase (function ‘Amp-T, Holland and Blundy 1994a’).  
449 Crystallization *T* for amphibole were found to vary from 680±6°C in contact with  
450 Jd<sub>30%</sub> clinopyroxene to 640±8°C in contact with Jd<sub>10%</sub> clinopyroxene. This

451 relationship was used to calculate the  $T$  of clinopyroxene.  $P$  for clinopyroxene  
452 crystallization were subsequently calculated using the calibration of Waters (2003) for  
453 the equilibrium reaction:  $\text{jad} + \text{trem} = \text{alb} + \text{ed}$ .

454 About 165 000  $P$ - $T$  calculations (one for each Cpx pixels) have been obtained and the  
455 results have been plotted into binary diagrams (Fig. 9a and 9b) using the module  
456 Chem2D, and into  $P$  and  $T$  maps (Fig. 9c and Fig. 9d). The density  $P$ - $T$  diagram  
457 option (Fig. 9b) plotted using the Chem2D module shows that the apparent deviation  
458 in  $P$  is composed of a small proportion of points ( $< 1\%$ ). In contrast, the density  
459 diagram shows a significant trend for  $T$  and  $P$  corresponding to the prograde evolution  
460 from  $650^{\circ}\text{C}$  to  $750^{\circ}\text{C}$  and from 24 kbar to 25 kbar. This increase in  $T$  and the slight  
461 increase of  $P$  along the prograde path is confirmed by the spatial distribution of the  
462 obtained  $T$  and  $P$  when plotted on a map: omphacite grains show high  $P$  at  $\sim 25$  kbar,  
463 and are zoned in  $T$  from  $650^{\circ}\text{C}$  in the old grain cores to  $750^{\circ}\text{C}$  in the old grain rims.  
464 Clinopyroxene in the symplectite shows a different trend with a decrease of both  $P$   
465 and  $T$  with the decreasing size of the intergrowths (Fig. 9). This interpretation on the  
466 preservation of  $P$  and  $T$  in symplectite during the exhumation is in good agreement  
467 with the reported high cooling rates (Guillot et al., 2009). This example typifies the  
468 importance of the mapping approach, which allows to test for relationships between  
469  $P$ - $T$  conditions and the textural information from metamorphic microstructures.

470

#### 471 **4. Concluding remarks**

472 This paper describes XMapTools, a MATLAB©-based GUI program to quantify raw  
473 X-ray electron microprobe data using internal standards, plot chemical diagrams and  
474 calculate  $P$ - $T$  conditions of crystallization for metamorphic parageneses. The  
475 XMapTools program includes 15 user-friendly main functions for the different steps

476 to the procedure, from the loading of the raw data to calculating  $P$ - $T$  maps, and two  
477 external modules *Chem2D* and *TriPlot3D* with independent graphical user interfaces  
478 to plot chemical diagrams. Beside the treatment of compositional maps, XMapTools  
479 offers the possibility of estimating thermobarometric conditions, which can be linked  
480 to the observed deformation features. For the study of metamorphic and magmatic  
481 rocks, a set of external functions specific to geothermobarometry is also included.  
482 This set comprises a range of structural formulae functions for usual rock-forming  
483 silicate minerals as well as empirical and semi-empirical geothermobarometers from  
484 the literature. Application of XMapTools to an eclogite sample shows that the  
485 accuracy of the mapped minerals composition is good enough to discuss the  
486 compositional-structural- $P$ - $T$  relationships based from Na distribution in  
487 clinopyroxene. A strong link between metamorphic textures and composition has  
488 been found, and the retrieved  $P$ - $T$  information gives a detailed reconstruction of the  
489 metamorphic history of the sample.

490 A more detailed thermobarometric study can be made using independent programs  
491 such as e.g. Theriak-Domino (de Capitani and Petrakakis 2010) or Tweep (Berman,  
492 2007) with the whole range of mineral compositions derived from XMapTools, which  
493 can be easily exported to the required formats. Moreover, an interesting feature of  
494 XMapTools is the possibility to calculating local bulk rock compositions from  
495 selected parts of the 2D maps. Such compositions can be used to calculate the stable  
496 mineral assemblages, compositions and abundance by free energy minimizing (e.g.  
497 Powell, 2008), and to compare them with the observed features. This approach,  
498 illustrated in Lanari et al. (2013) for the example discussed in the present  
499 contribution, can provide valuable information on the degree of achievement of  
500 thermodynamic equilibrium, the link between deformation and reequilibration, and

501 possibly the extend of mass transfer controlled by deformation. Future release of  
502 XMapTools will incorporate energy minimizing and multi-equilibrium modules to  
503 facilitate advanced thermobarometric studies.

504

## 505 **5. Acknowledgements**

506 Authors acknowledge A. Pourteau for his help with the EPMA analyses, N. Riel, C.  
507 Martin, F. Guillot, B. Gardonio, F. Bernier, M. Engi, M. Muñoz, K. Malamoud, A.  
508 Robert, J. de Sigoyer, P. Agard and S. Guillot for help, comments, data and/or  
509 collaborations in order to test the different versions of XMapTools. Authors thank G.  
510 Ortolano, D. Waters and one anonymous reviewers for constructive comments and Jef  
511 Caers for editorial handling. This work was supported by the French ANR project  
512 “ERD-Alps”.

513

## 514 **6. References**

- 515 Ai, Y., 1994. A revision of the garnet-clinopyroxene  $\text{Fe}^{2+}$ -Mg exchange geothermometer. *Contrib. Min.*  
516 *Petrol.* 115(4), 467–473
- 517 Anderson, J.L., Smith, D.R., 1995. The effects of temperature and  $f_{\text{O}_2}$  on the Al-in-hornblende  
518 barometer. *Am. Min.* 80, 549–559.
- 519 Bence, A.E. and Albee, A.E., 1968. Empirical correction factors for the electron microanalysis of  
520 silicates and oxides. *Journal of Geology.* 76, 382-403.
- 521 Berman, R.G., 1991. Thermobarometry using multi-equilibrium calculations: a new technique, with  
522 petrological applications. *Can. Min.* 29, 833–855.
- 523 Berman R. G. 2007. WinTWQ (version 2.3) a software package for performing internally-consistent  
524 thermobarometric calculations. Geological Survey of Canada pp. 41.
- 525 Blundy, J.D., Holland, T.J.B., 1990. Calcic amphibole equilibria and a new amphibole-plagioclase  
526 geothermometer. *Contrib. Min. Petrol.* 104, 208–224.
- 527 Bonnet, N. (1998). Multivariate statistical methods for the analysis of microscope image series:  
528 applications in material science. *Journal of Microscopy.* 190, 2-18.
- 529 Castaing, R., 1951. Application des sondes electronique a une methode d’analyse ponctuelle chimique  
530 et cristallographique. Université de Paris (publication ONERA), Paris.
- 531 Cathelineau, M., 1988. Cation site occupancy in chlorites and illites as function of temperature. *Clay*  
532 *Min.* 23, 471–485.
- 533 Cathelineau, M., Nieva, D., 1985. A chlorite solid solution geothermometer the Los Azufres (Mexico)

- 534 geothermal system. *Contrib. Min. Petrol.* 91, 235–244.
- 535 Clarke, G.L., Daczko, N.R. and Nockolds, C. 2001. A method for applying matrix corrections to X-ray  
536 intensity maps using the Bence-Albee algorithm and Matlab. *J. Metam. Geol.* 19, 653–644.
- 537 Coggon, R., Holland, T., 2002. Mixing properties of phengitic micas and revised garnet-phengite  
538 thermobarometers. *J. Metam. Geol.* 20, 683–696.
- 539 Cossio, R., Borghi, A., Ruffini, R. (2002) Quantitative modal determination of geological samples  
540 based on X-ray multielemental map acquisition. *Microsc. Microanal.* 8, 139–149.
- 541 Cosslett, V.E. and Duncumb, P. (1956). Microanalysis by a flying-spot X-ray method. *Nature.* 177,  
542 1172–1173.
- 543 Creighton, S., 2009. A semi-empirical manganese-in-garnet single crystal thermometer. *Lithos* 112,  
544 177–182.
- 545 Dahl, P.S., 1980. The thermal-compositional dependence of Fe<sup>2+</sup>-Mg distributions between coexisting  
546 garnet and pyroxene: applications to geothermometry. *Am. Min.* 65(85), 866.
- 547 Dale, J., Holland, T., Powell, R., 2000. Hornblende–garnet–plagioclase thermobarometry: a natural  
548 assemblage calibration of the thermodynamics of hornblende. *Contrib. Min. Petrol.* 140, 353–  
549 362.
- 550 Dale, J., Powell, R., White, R., Elmer, F., Holland, J., 2005. A thermodynamic model for Ca–Na  
551 clin amphiboles in Na<sub>2</sub>O–CaO–FeO–MgO–Al<sub>2</sub>O<sub>3</sub>–SiO<sub>2</sub>–H<sub>2</sub>O–O for petrological calculations.  
552 *J. Metam. Geol.* 23, 771–791.
- 553 De Andrade, V., Vidal, O., Lewin, E., O'Brien, P., Agard, P., 2006. Quantification of electron  
554 microprobe compositional maps of rock thin sections: an optimized method and examples. *J.*  
555 *Metam. Geol.* 24, 655–668.
- 556 de Capitani C. and Petrakakis K. (2010): The computation of equilibrium assemblage diagrams with  
557 Theriak/Domino software. *Am. Min.* 95, 1006–1016
- 558 Dickenson, M., Hewitt, D., 1986. A garnet-chlorite geothermometer. *Geol. Soc. Am. Abstr.* 18, 584.
- 559 Dubacq, B., Vidal, O., Andrade, V., 2010. Dehydration of dioctahedral aluminous phyllosilicates:  
560 thermodynamic modelling and implications for thermobarometric estimates. *Contrib. Min.*  
561 *Petrol.* 159, 159–174.
- 562 Ellis, D., Green, D., 1979. An experimental study of the effect of Ca upon garnet-clinopyroxene Fe-Mg  
563 exchange equilibria. *Contrib. Min. Petrol.* 71, 13–22.
- 564 Fiannacca, P., Lo Po, D., Ortolano, G., Cirrincione, R., Pezzino, A., 2012. Thermodynamic modeling  
565 assisted by multivariate statistical image analysis as a tool for unraveling metamorphic P-T-s  
566 evolution: an example from ilmenite-garnet-bearing metapelite of the Peloritani Mountains,  
567 Southern Italy. *Miner. Petrol.* 106, 151–171.
- 568 Friel J.J. and Lyman, 2006. X-ray mapping in electron-beam instruments. *Microsc. Microanal.* 12, 2-  
569 25.
- 570 Ganguly, J., 1979. Garnet and clinopyroxene solid solutions, and geothermometry based on Fe-Mg  
571 distribution coefficient. *Geo. Cosmo. Acta.* 43(7), 1021–1029.
- 572 Ganne, J., De Andrade, V., Weinberg, R.F., Vidal, O., Dubacq, B., Kagambega, N., Naba, S.,  
573 Baratoux, L., Jessell, M., Allibon, J., 2012. Modern-style plate subduction preserved in the  
574 Palaeoproterozoic West African craton. *Nature Geoscience* 5, 60–65.
- 575 Goldman, D., Albee, A., 1977. Correlation of Mg/Fe partitioning between garnet and biotite with  
576 O<sub>18</sub>/O<sub>16</sub> partitioning between quartz and magnetite. *Am. J. Sc.* 277, 750–761.

- 577 Graham, C. & Powell, R., 1984. A garnet-hornblende geothermometer: calibration, testing, and  
578 application to the Pelona Schist, Southern California. *J. Metam. Geol.* 2(1), 13–31.
- 579 Grambling, J.A., 1990. Internally-consistent geothermometry and H<sub>2</sub>O barometry in metamorphic  
580 rocks: the example garnet-chlorite-quartz. *Contrib. Min. Petrol.* 105, 617–628.
- 581 Green, T., Hellman, P., 1982. Fe-Mg partitioning between coexisting garnet and phengite at high  
582 pressure, and comments on a garnet-phengite geothermometer. *Lithos* 15, 253–266.
- 583 Guillot, S., Riel, N., Hattori, K., Desgreniers, S., Rolland, Y., Van Melle, J., Latif, M., Kausar, A.,  
584 Pêcher, A., 2008. New occurrence of eclogitic continental rocks in NW Himalaya: The Stak  
585 massif in northern Pakistan. *Himalayan journal of sciences* 5, 57–58.
- 586 Guillot, S. Hattori, K., Agard, P., Schwartz, S., Vidal, O. (2009) Exhumation processes in oceanic and  
587 continental subduction contexts : a review. In S. Lallemand and F. Funiciello (eds.) *Subduction  
588 Zone Dynamics*, 175-204, doi 10.1007/978-3-540-87974-9, Springer-Verlag Berlin Heidelberg.
- 589 Hammarstrom, J., Zen, E., 1986. Aluminum in hornblende; an empirical igneous geobarometer. *Am.*  
590 *Min.* 71, 1297–1313.
- 591 Hillier, S., Velde, B., 1991. Octahedral occupancy and chemical composition of diagenetic (low-  
592 temperature) chlorites. *Clay Min.* 26, 149.
- 593 Holdaway, M., Lee, S., 1977. Fe-Mg cordierite stability in high-grade pelitic rocks based on  
594 experimental theoretical and natural observations. *Contrib. Min. Petrol.* 63, 175–17198.
- 595 Holland, T., Baker, J., Powell, R., 1998. Mixing properties and activity-composition and relationships  
596 of chlorites in the system MgO-FeO-Al<sub>2</sub>O<sub>3</sub>-SiO<sub>2</sub>-H<sub>2</sub>O. *Eur. J. Min.* 10, 395-406.
- 597 Holland, T., Blundy, J., 1994. Non-ideal interactions in calcic amphiboles and their bearing on  
598 amphibole-plagioclase thermometry. *Contrib. Min. Petrol.* 116, 433–447.
- 599 Holland, T., Powell, R., 1998. An internally consistent thermodynamic data set for phases of  
600 petrological interest. *J. Metam. Geol.* 16, 309–343.
- 601 Holland, T., Powell, R., 2011. An improved and extended internally consistent thermodynamic dataset  
602 for phases of petrological interest, involving a new equation of state for solids. *J. Metam. Geol.*  
603 29, 333–383.
- 604 Hollister, L.S., Grissom, G., Peters, E., Stowell, H., Sisson, V., 1987. Confirmation of the empirical  
605 correlation of Al in hornblende with pressure of solidification of calc-alkaline plutons. *Am.*  
606 *Min.* 72, 231.
- 607 Inoue, A., Meunier, A., Patrier-Mas, P., Rigault, C., Beaufort, D., Vieillard, P., 2009. Application of  
608 Chemical Geothermometry to Low-Temperature Trioctahedral Chlorites. *Clays and Clay Min.*  
609 57, 371–382.
- 610 Joanny, V., van Roermund, H., Lardeaux, J.M., 1991. The clinopyroxene/plagioclase symplectite in  
611 retrograde eclogites: a potential geothermobarometer. *Geologische Rundschau* 80(2), 303-320.
- 612 Johnson, M., Rutherford, M., 1989. Experimental calibration of the aluminum-in-hornblende  
613 geobarometer with application to Long Valley valdera (California) volcanic rocks. *Geology* 17,  
614 837–841.
- 615 Jowett, E., 1991. Fitting iron and magnesium into the hydrothermal chlorite geothermometer:  
616 GAC/MAC/SEG, Presented at the Joint Annual Meeting (Toronto, May 27-29, 1991) Program  
617 with Abstracts.
- 618 Kawasaki, T., Nakano, N., Osanai, Y., 2011. Osumilite and a spinel+quartz association in garnet-  
619 sillimanite gneiss from Rundvågshetta, Lützow-Holm Complex, East Antarctica. *Gondwana  
620 Research* 19, 430–445.
- 621 Kohn, M.J. and Spear, F., 2000. Retrograde net transfer reaction insurance for pressure-temperature



- 622 estimates. *Geology* 28, 1127-1130.
- 623 Kranidiotis, P., MacLean, W., 1987. Systematics of chlorite alteration at the Phelps Dodge massive  
624 sulfide deposit, Matagami, Quebec. *Economic Geology and the Bulletin of Society of Economic*  
625 *Geologists* 82, 1898–1911.
- 626 Krogh, E.J., Råheim, A., 1978. Temperature and pressure dependence of Fe-Mg partitioning between  
627 garnet and phengite, with particular reference to eclogites. *Contrib. Min. Petro.* 66, 75–80.
- 628 Krogh, E.J., 1988. The garnet-clinopyroxene Fe-Mg geothermometer a reinterpretation of existing  
629 experimental data. *Contrib. Min. Petro.* 99(1), 44–48.
- 630 Lanari, P., Guillot, S., Schwartz, S., Vidal, O., Tricart, P., Riel, N., Beyssac, O., 2012. Diachronous  
631 evolution of the alpine continental subduction wedge: Evidence from P–T estimates in the  
632 Briançonnais Zone houillère (France – Western Alps). *J. Geodynamics* 56-57, 39–54.
- 633 Lanari, P., Riel, N., Guillot, S., Vidal, O., Schwartz, S., Pêcher, A., Hattori, K. (2013). Deciphering  
634 High-Pressure metamorphism in collisional context using microprobe-mapping methods:  
635 application to the Stak eclogitic massif (NW Himalaya). *Geology*, 41, 111-114.
- 636 Launeau, P., Cruden, A.R., and Bouchez, J.L. (1994) Mineral recognition in digital images of rocks: a  
637 new approach using multichannel classification. *Can. Min.* 32, 919–933.
- 638 Massone, H., Schreyer, W., 1987. Phengite geobarometry based on the limiting assemblage with K-  
639 feldspar, phlogopite and quartz. *Contrib. Min. Petrol.* 96, 212–224.
- 640 Mori, T. & Green, D., 1978. Laboratory duplication of phase equilibria observed in natural garnet  
641 lherzolites. *J. Geol.* 86, 83–97.
- 642 Muñoz, M., De Andrade, V., Vidal, O., Lewin, E., Pascarelli, S., Susini, J., 2006. Redox and speciation  
643 micromapping using dispersive X-ray absorption spectroscopy: Application to iron in chlorite  
644 mineral of a metamorphic rock thin section. *Geochem. Geophys. Geosyst.* 7(11) 1-10.
- 645 Mysen, B. and Heier, K., 1972. Petrogenesis of eclogites in high grade metamorphic gneisses,  
646 exemplified by the Hareidland eclogite, western Norway. *Contrib. Min. Petrol.* 36(1), 73–94.
- 647 Pattison, D. R. M., and Newton, R. C., 1989, Reversed experimental calibration of the garnet-  
648 clinopyroxene Fe-Mg exchange thermometer: *Contrib. Min. Petrol.* 101, 87-103.
- 649 Parra, T., Vidal, O., Agard, P., 2002. A thermodynamic model for Fe–Mg dioctahedral K white micas  
650 using data from phase-equilibrium experiments and natural pelitic assemblages. *Contrib. Min.*  
651 *Petrol.* 143, 706–732.
- 652 Perchuk, L., Aranovich, L.Y., Podlesskii, K., Lavrent'eva, I., Gerasimov, V., Fed'kin, V., Kitsul, V.,  
653 Karsakov, L., Bernikov, N., 1985. Precambrian granulites of the Aldan shield, eastern Siberia,  
654 USSR. *J. Metam. Geol.* 3, 265–310.
- 655 Plunder, A., Agard, P., Dubacq, B., Chopin, C., Bellanger, M., 2012. How continuous and precise is  
656 the record of P-T paths? Insights from combined thermobarometry and thermodynamic  
657 modelling into subduction dynamics (Schistes Lustrés, W. Alps). *J. Metam. Geol.* 30, 323-346.
- 658 Powell, R., 1985. Regression diagnostics and robust regression in geothermometer/geobarometer  
659 calibration: the garnet-clinopyroxene geothermometer revisited. *J. Metam. Geol.* 3, 231–243.
- 660 Powell R. 2008. On thermobarometry. *J. Metam. Geol.* 26, 155–179.
- 661 Pourteau, L., Sudo, M., Candan, O., Lanari, P., Vidal, O., Oberhänsli, R. (2013). Neotethys closure  
662 history of Anatolia: insights from <sup>40</sup>Ar–<sup>39</sup>Ar geochronology and P–T estimation in high  
663 pressure metasedimentary rocks. *J. Metam. Geol.* doi:10.1111/jmg.12034.
- 664 Prêt, D., Sammartino, S., Beaufort, D., Meunier A., Fialin, M., Michot, L.J. (2010). A new method for  
665 quantitative petrography based on image processing of chemical element maps: Part I. Mineral  
666 mapping applied to compacted bentonites. *Am. Min.* 95, 1379-1388.

- 667 Råheim, A., Green, D.H., 1974. Experimental determination of the temperature and pressure  
668 dependence of the Fe-Mg partition coefficient for coexisting garnet and clinopyroxene. *Contrib.*  
669 *Min. Petrol.* 48, 179–203.
- 670 Ravna, E.K., 2000a. The garnet–clinopyroxene Fe<sup>2+</sup>–Mg geothermometer: an updated calibration. *J.*  
671 *Metam. Geol.* 18, 211–219.
- 672 Ravna, E.K., 2000b. Distribution of Fe<sup>2+</sup> and Mg between coexisting garnet and hornblende in  
673 synthetic and natural systems: an empirical calibration of the garnet-hornblende Fe-Mg  
674 geothermometer. *Lithos* 53, 265–277.
- 675 Reed, S.J.B. 2005. *Electron microprobe analysis and scanning electron microscopy in geology.* 2<sup>nd</sup>  
676 edition, Cambridge University Press.
- 677 Riel, N., Hattori, K., Guillot, S., Rayner, N., Davis, N., Latif, M., Kausar, M., 2008, SHRIMP zircon  
678 ages of eclogites in the Stak massif, northern Pakistan: *Himalayan Journal of Sciences*, 5, 119–  
679 120.
- 680 Saporta, G., 1990. *Probabilités, analyse des données et statistique.* Editions Technip, Paris.
- 681 Schmidt, M.W., 1992. Amphibole composition in tonalite as a function of pressure: an experimental  
682 calibration of the Al-in-hornblende barometer. *Contrib. Min. Petrol.* 110, 304–310.
- 683 Seber, G., 1984. *Multivariate Observations.* Hoboken, NJ: John Wiley & Sons, Inc.
- 684 Sengupta, P., Dasgupta, S., Bhattacharya, P. K., and Hariya, Y., 1989, Mixing behavior in quaternary  
685 garnet solid solution and an extended Ellis and Green garnet-clinopyroxene geothermometer.  
686 *Contrib. Min. Petrol.* 103, 223-227.
- 687 Spath, H., 1985. *Cluster dissection and analysis: theory, FORTRAN programs, examples.* New York:  
688 Halsted Press.
- 689 Spear, F., 1995. *Metamorphic phase equilibria and Pressure-Temperature-time paths.* Mineral Society  
690 of America, Washington.
- 691 Thompson, A., 1976. Mineral reactions in pelitic rocks: II. Calculation of some P-T-X(Fe-Mg) phase  
692 relations. *Am. J. Sc.* 276, 425–454.
- 693 Tinkham, D.K., Ghent, E.D., 2005. XRMMapAnal: A program for analysis of quantitative X-ray maps.  
694 *Am. Min.* 90, 737-744.
- 695 Vidal, O., Parra, T., 2000. Exhumation paths of high-pressure metapelites obtained from local  
696 equilibria for chlorite–phengite assemblages. *Geol. J.* 35, 139–161.
- 697 Vidal, O., Goffé, B., Bousquet, R., Parra, T., 1999. Calibration and testing of an empirical  
698 chloritoid-chlorite Mg-Fe exchange thermometer and thermodynamic data for daphnite. *J.*  
699 *Metam. Geol.* 17, 25–39.
- 700 Vidal, O., Parra, T., Trotet, F., 2001. A Thermodynamic Model for Fe-Mg Aluminous Chlorite Using  
701 Data from Phase Equilibrium Experiments and Natural Pelitic Assemblages in the 100 to 600°C,  
702 1 to 25 kb Range. *Am. J. Sc.* 301, 557.
- 703 Vidal, O., Parra, T., Vieillard, P., 2005. Thermodynamic properties of the Tschermak solid solution in  
704 Fe-chlorite: Application to natural examples and possible role of oxidation. *Am. Min.* 90, 347–  
705 358.
- 706 Vidal, O., De Andrade, V., Lewin, E., Munoz, M., Parra, T., Pascarelli, S., 2006. P-T-deformation-  
707 Fe<sup>3+</sup>/Fe<sup>2+</sup> mapping at the thin section scale and comparison with XANES mapping: application  
708 to a garnet-bearing metapelite from the Sambagawa metamorphic belt (Japan). *J. Metam. Geol.*  
709 24, 669–683.
- 710 Warren, C., Waters, D., 2006. Oxidized eclogites and garnet-blueschists from Oman: P–T path

- 711 modelling in the NCFMASHO system. *J. Metam. Geol.* 24, 1–20.
- 712 Waters, D., 1996. The Garnet-Cpx-Phengite barometer. Recommended calibration and calculation  
713 method, updated 1 March 1996. ([http:](http://www.earth.ox.ac.uk/~davewa/research/eclogite/ecbarcal.html)  
714 [//www.earth.ox.ac.uk/~davewa/research/eclogite/ecbarcal.html](http://www.earth.ox.ac.uk/~davewa/research/eclogite/ecbarcal.html) 1).
- 715 Waters, D., 2002. Clinopyroxene-Amphibole-plagioclase symplectites in Norwegian eclogites:  
716 microstructures, chemistry and the exhumation P-T path. Mineralogical Society, Winter  
717 Conference, Derby.
- 718 Waters, D., 2003. P-T paths from Cpx-Hbl-Pl symplectites, updated 22 February 2003.  
719 <http://www.earth.ox.ac.uk/~davewa/research/eclogites/symplectites.html>.
- 720 Waters, D., Martin, H., 1993. Geobarometry in phengite-bearing eclogites. *Terra Nova* 5, 410–411.
- 721 Yamato, P., Agard, P., Burov, E., Le Pourhiet, L., Jolivet, L., Tiberi, C., 2007. Burial and exhumation  
722 in a subduction wedge: Mutual constraints from thermomechanical modeling and natural P-T-t  
723 data (Schistes Lustrés, western Alps). *J. Geophys. Res.* 112, B07410.
- 724 Zack, T., Moraes, R., Kronz, A., 2004. Temperature dependence of Zr in rutile: empirical calibration of  
725 a rutile thermometer. *Contrib. Min. Petrol.* 148, 471–488.
- 726 Zang, W., Fyfe, W., 1995. Chloritization of the hydrothermally altered bedrock at the Igarape Bahia  
727 gold deposit, Carajas, Brazil. *Mineralium Deposita* 30, 30–38.
- 728
- 729
- 730

731 **Figure Caption**

732

733 **Fig. 1:** *XMapTools* v1.5.2 graphic user interface. The displayed image is the raw Al-  
734 content map of the sample 'Eclogite' (see text for details) unit: number of recorded  
735 counts.

736 **Fig. 2:** *XMapTools* operating diagram, schematizing the structure of the program. All  
737 steps marked with a star require user action. Light arrows indicate the way forward,  
738 bold-arrows the transition between the different sub-programs (Xray, Quanti, Results,  
739 see text), and the dashed arrows the available feedback.

740 **Fig. 3:** Intensity recorded on the map versus oxide weight percent concentrations for  
741 Si in the studied sample. Blue crosses show point analyses, lines are regressed  
742 calibration curves obtained using the median approach described in text. The  
743 precision is given depending on the intensity (% at  $2\sigma$ ) following equation 1 (see  
744 text).

745 **Fig. 4:** Results from the *XMapTools Chem2D* module. (A) The clinopyroxene  
746 compositions are plotted in a binary diagram Na vs Mg. Unit is per formula unit  
747 (p.f.u.). The pixels displayed in the map are colored in red. (B) Density map  
748 calculated from the binary diagram (see text for details). (C) Map of the analyzed area  
749 in which clinopyroxene pixels selected in A are in red and the unselected pixels in  
750 blue. Black pixels do not belong to the clinopyroxene mask. Selected Na-rich pixels  
751 correspond to 25% of the total clinopyroxene pixels.

752 **Fig. 5:** Results from the *XMapTools TriPlot3D* module. (A) Clinopyroxene  
753 compositions plotted in a ternary diagram jadeite-diopside-hedenbergite. Unit is the  
754 end-member proportion. The selected pixel groups displayed into a map in C are  
755 colored according to their group (blue: group 1, cyan: group 2, yellow: group 3). (B)

756 Density map calculated from the ternary diagram. (C) Map of the analyzed area, in  
757 which the selected groups of clinopyroxene pixels in A are plotted with the same  
758 colors as in A.

759 **Fig. 6:** Phase masks for the “eclogite” sample (A) computed using the ‘normalized’  
760 method (see text). The part used to compare the two available methods is marked  
761 using a dashed rectangle. (B) Comparison between the “classical” and “normalized”  
762 methods with a difference image in which black pixels are the pixels not allocated to  
763 the same groups with both methods.

764 **Fig. 7:** Na-content of clinopyroxene (including omphacite). The different stages of  
765 crystallization (labeled 1 to 4) are discussed in the text.

766 **Fig. 8:** Diagrams showing the difference between point analyses composition  
767 (standard) and the standardized composition on the same location on the X-ray maps  
768 for garnet and different elements. (A) SiO<sub>2</sub>, (B) Al<sub>2</sub>O<sub>3</sub>, (C) FeO, (D) CaO, (E) MgO,  
769 (F) MnO, (G) TiO<sub>2</sub>, (H) K<sub>2</sub>O, (I) Na<sub>2</sub>O. *BDL*: below detection limit.

770 **Fig. 9:** P-T path and P-T maps of the Stak sample estimated from the compositions of  
771 clinopyroxenes (see text for details). The interpreted *P-T* path is from Lanari et al.  
772 (2013).

773

774

775 **Table captions**

776

777 **Table 1:** List of solid-solution models and associated end-members included in  
778 XMapTools.

779 **Table 2:** List of exchange reaction calibrations included in XMapTools.

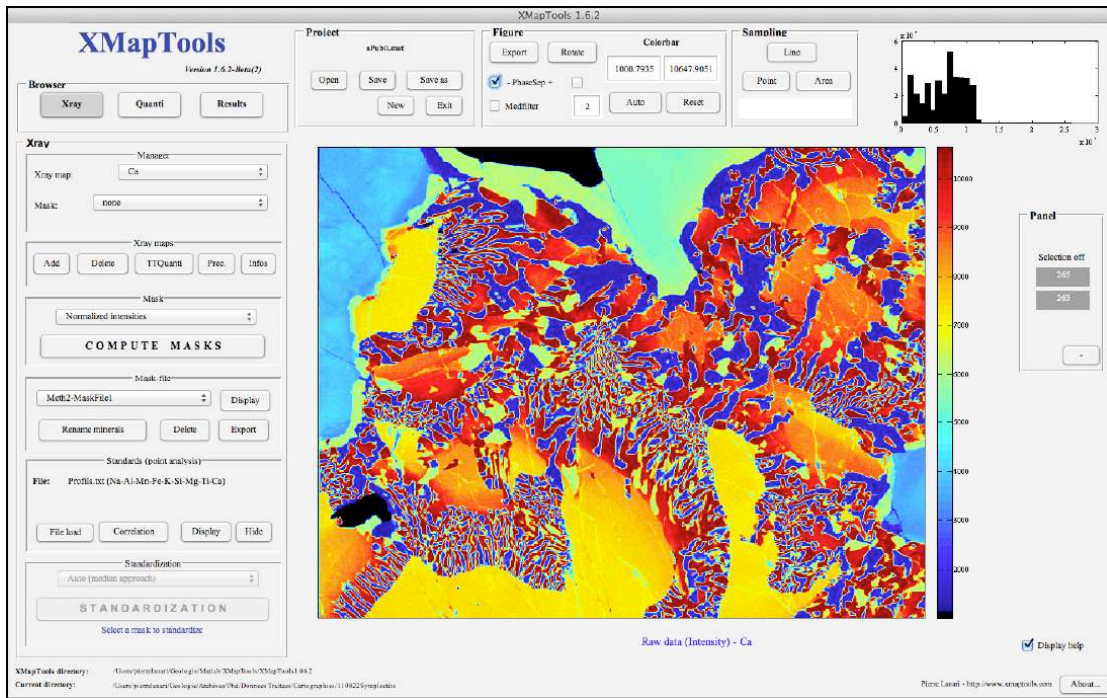
780 **Table 3:** List of empirical thermometers, barometers and multi-equilibrium functions  
781 implemented in XMapTools.

782 **Table 4:** Phase proportions (volume %) estimated with XMapTools using the  
783 available methods ‘normalized’ and ‘classical’. The difference in percentage is an  
784 absolute difference.

785 **Table 5:** Uncertainties resulting from microprobe acquisition on raw data and error-  
786 propagation using Monte-Carlo techniques on quantified data and structural formulae  
787 for clinopyroxene. The precision at  $2\sigma$ -level on raw data (in %) was estimated using  
788 the equation 2 (see text) on the average intensity of all the pixels of clinopyroxene.  
789 This uncertainty was propagated on the quantification process using a Monte-Carlo  
790 simulation with  $n=100\ 000$  analyses. The uncertainty was similarly propagated on the  
791 structural formulae calculation process, including atom-site distribution.

792

Figure 1

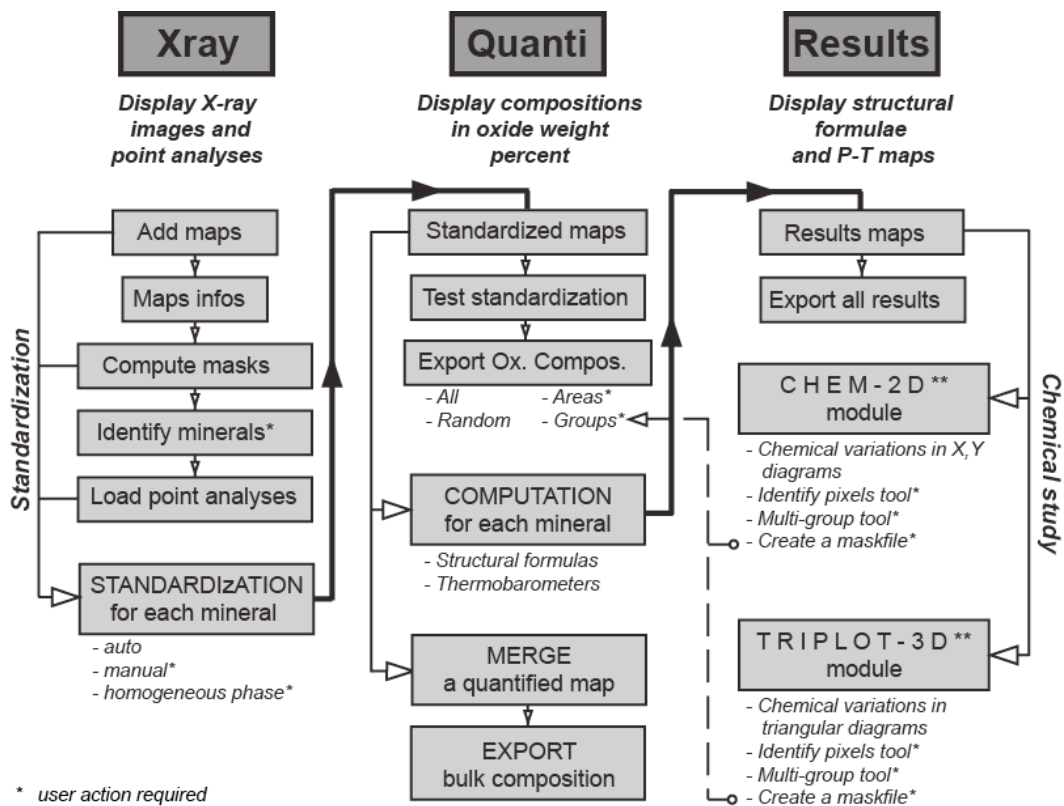


794

795

796

Figure 2

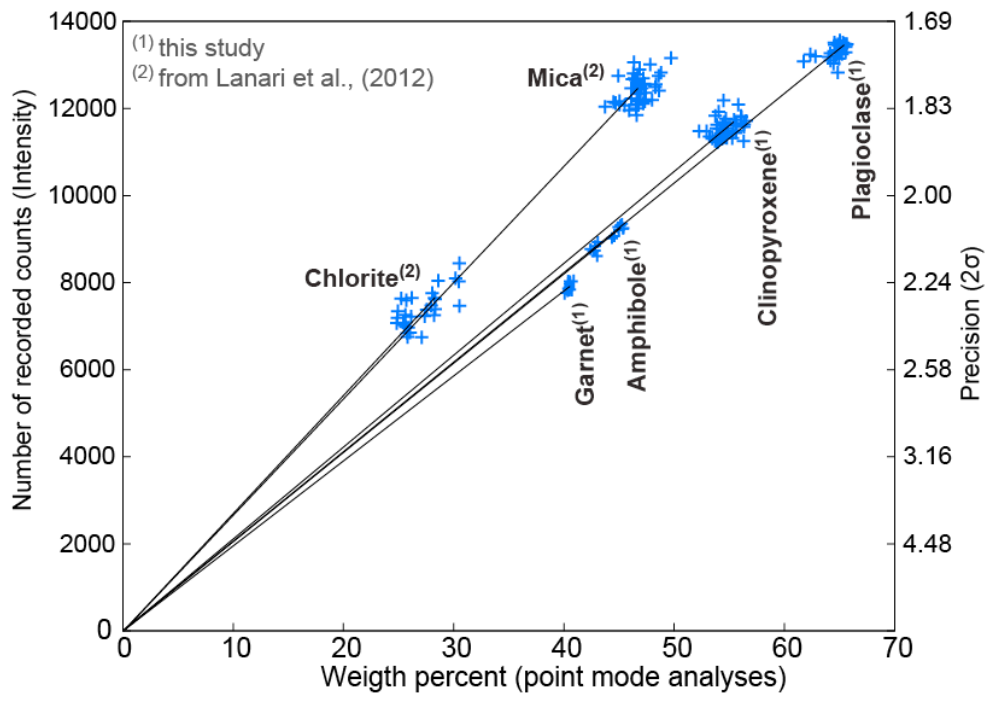


\* user action required  
 \*\* external GUI modules

797

798

Figure 3



800

801

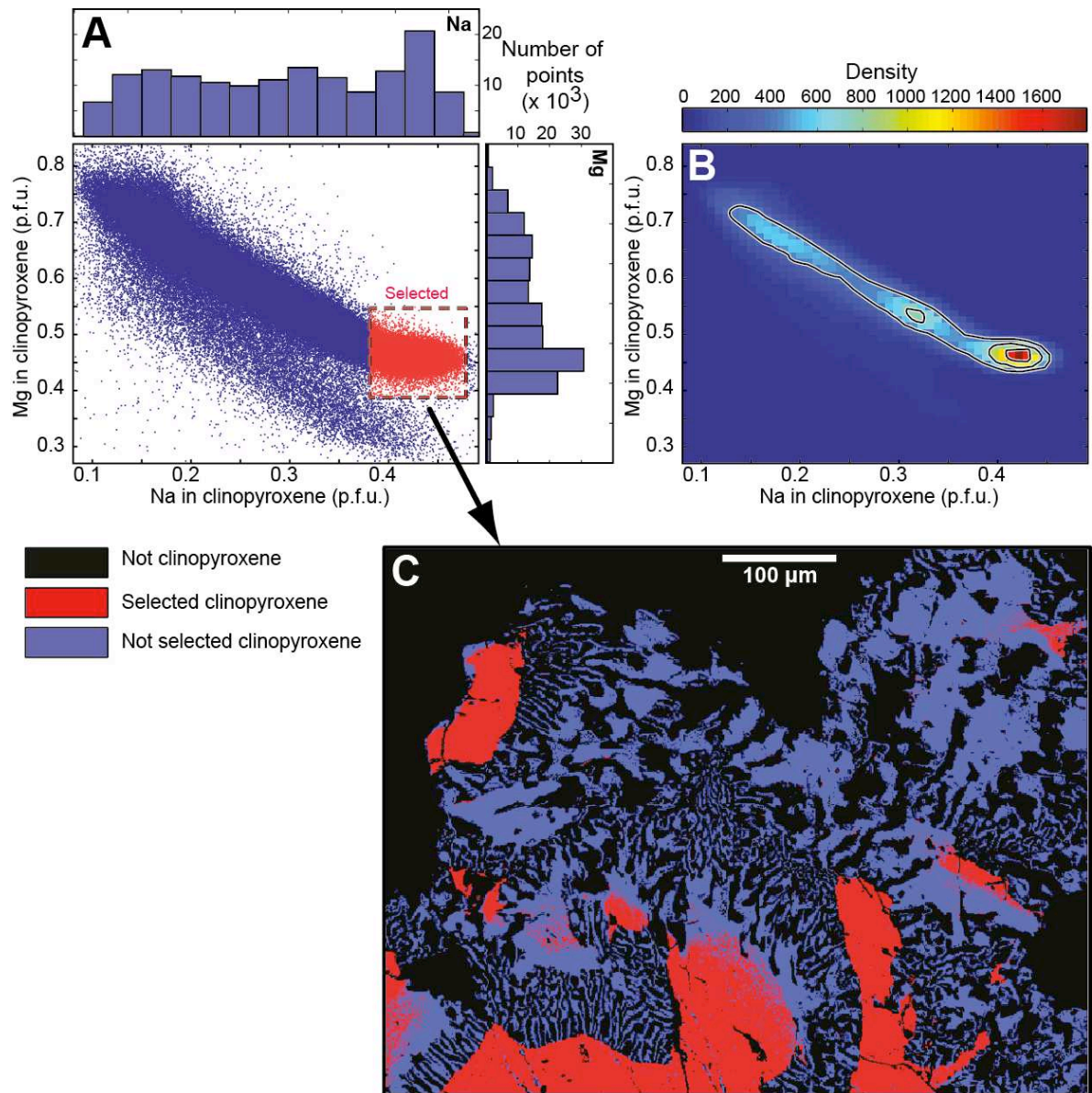
802



803

Figure 4

804



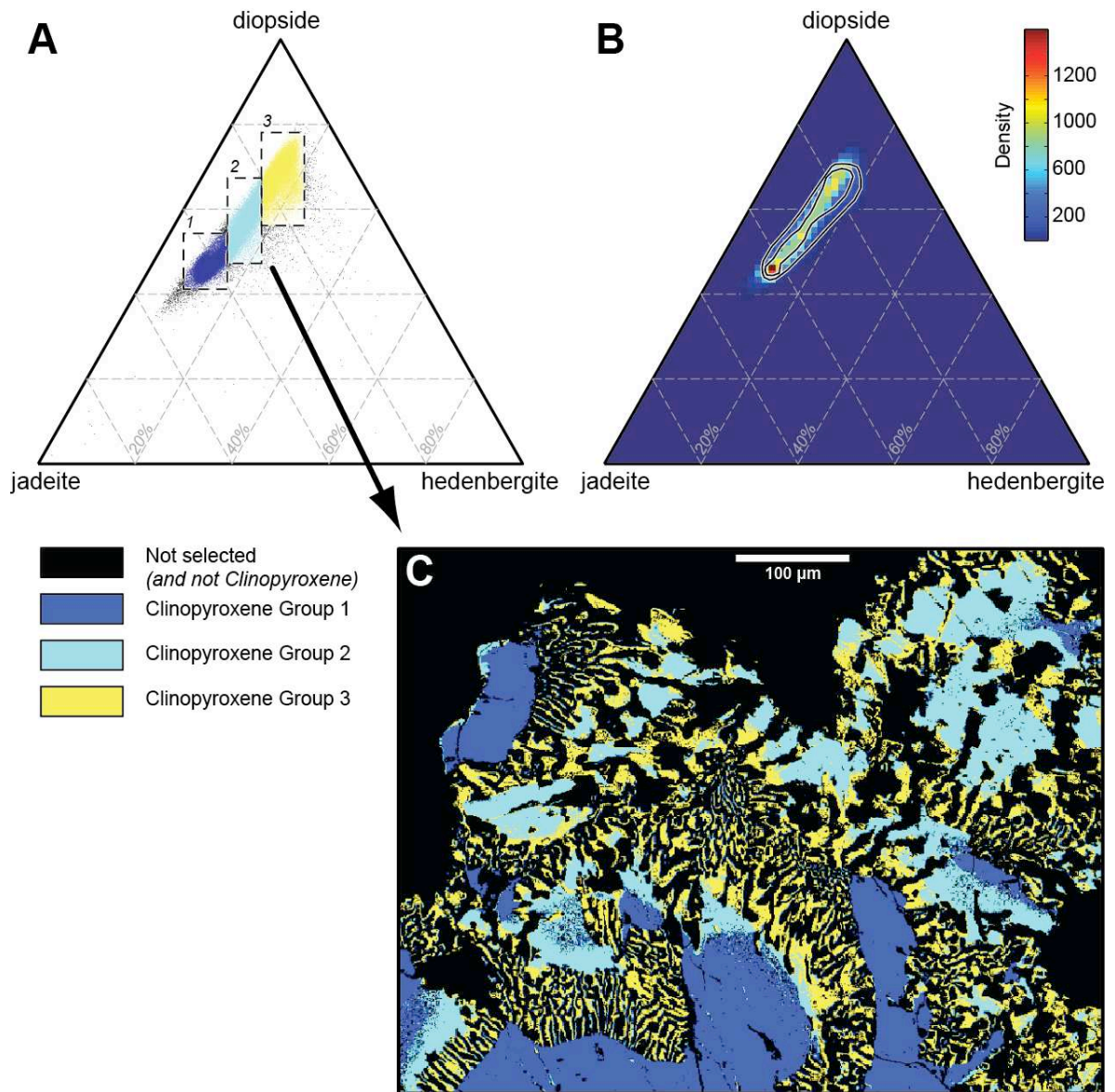
805

806

807

Figure 5

808



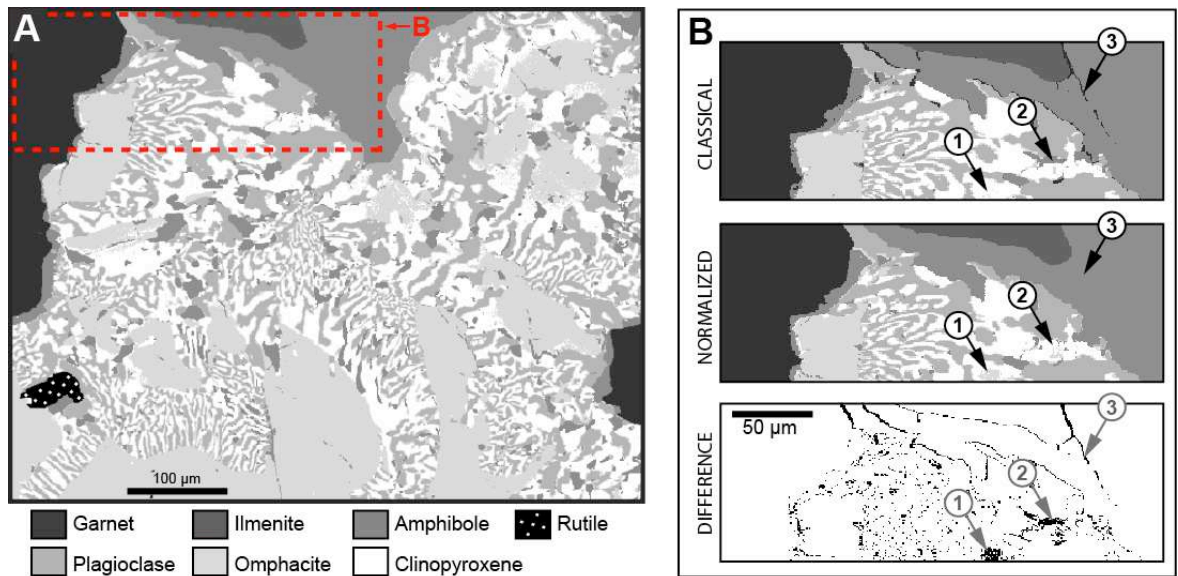
809

810

811

Figure 6

812



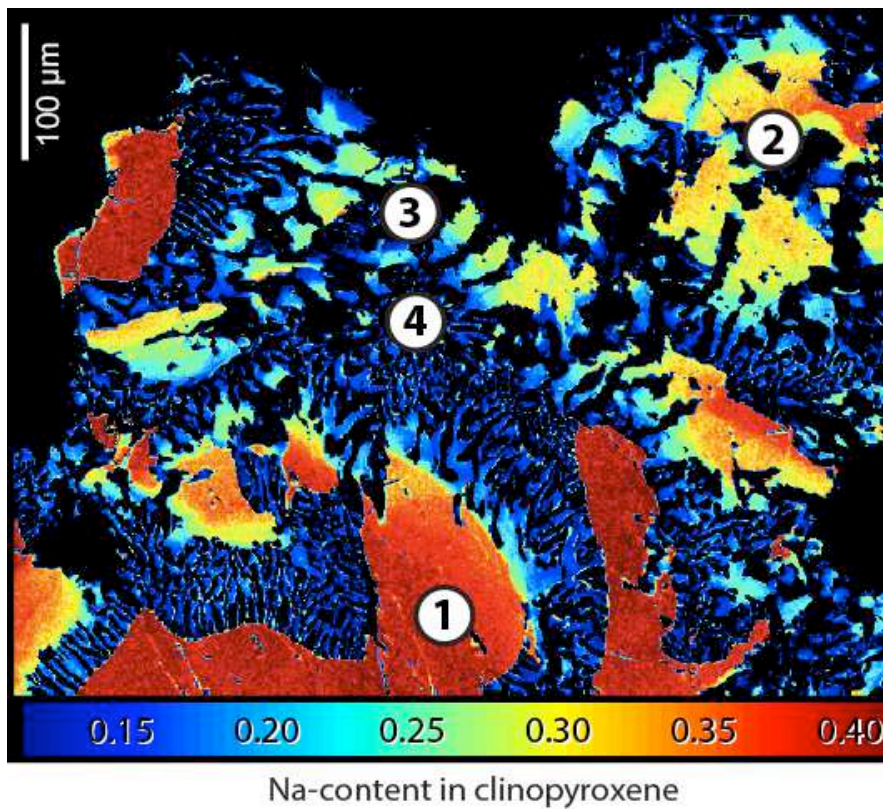
813

814

815

816

Figure 7



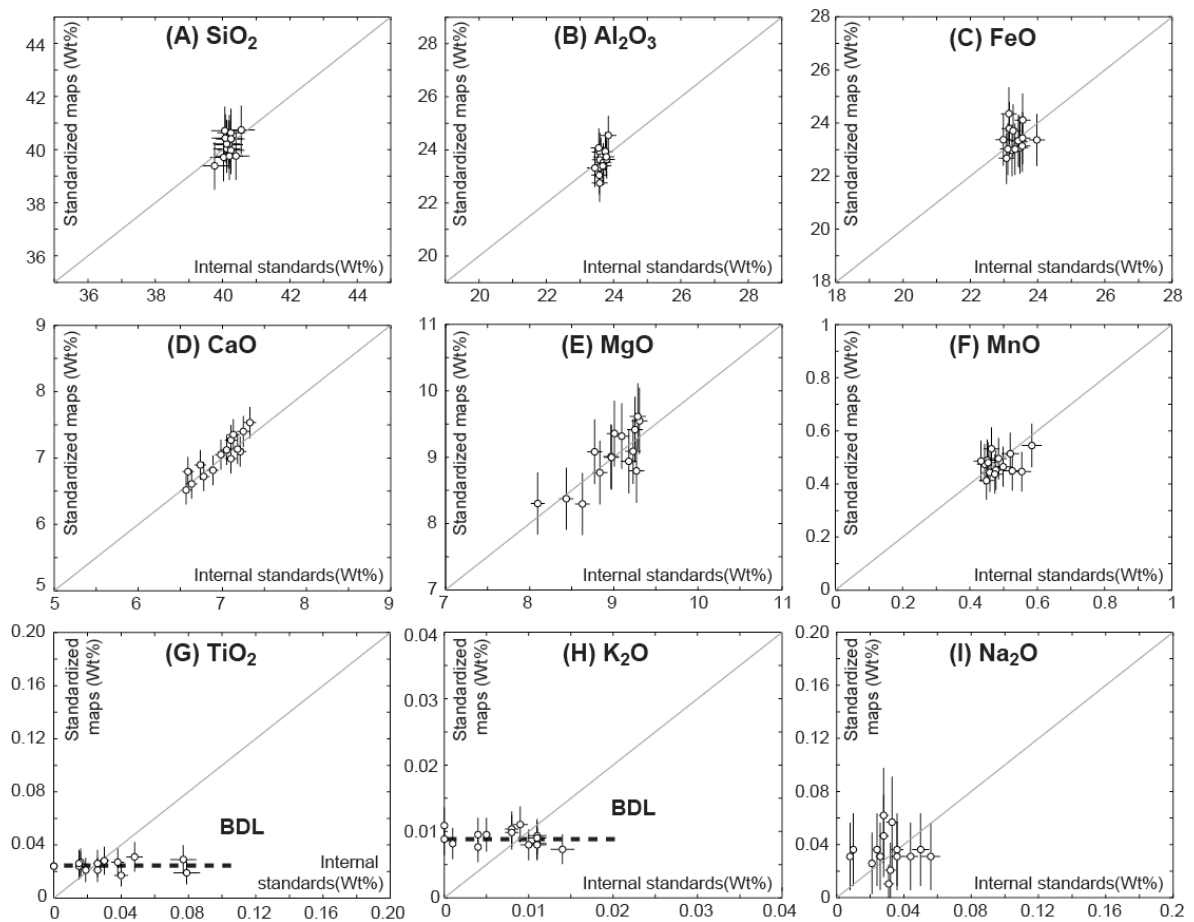
817

818

819

Figure 8

820



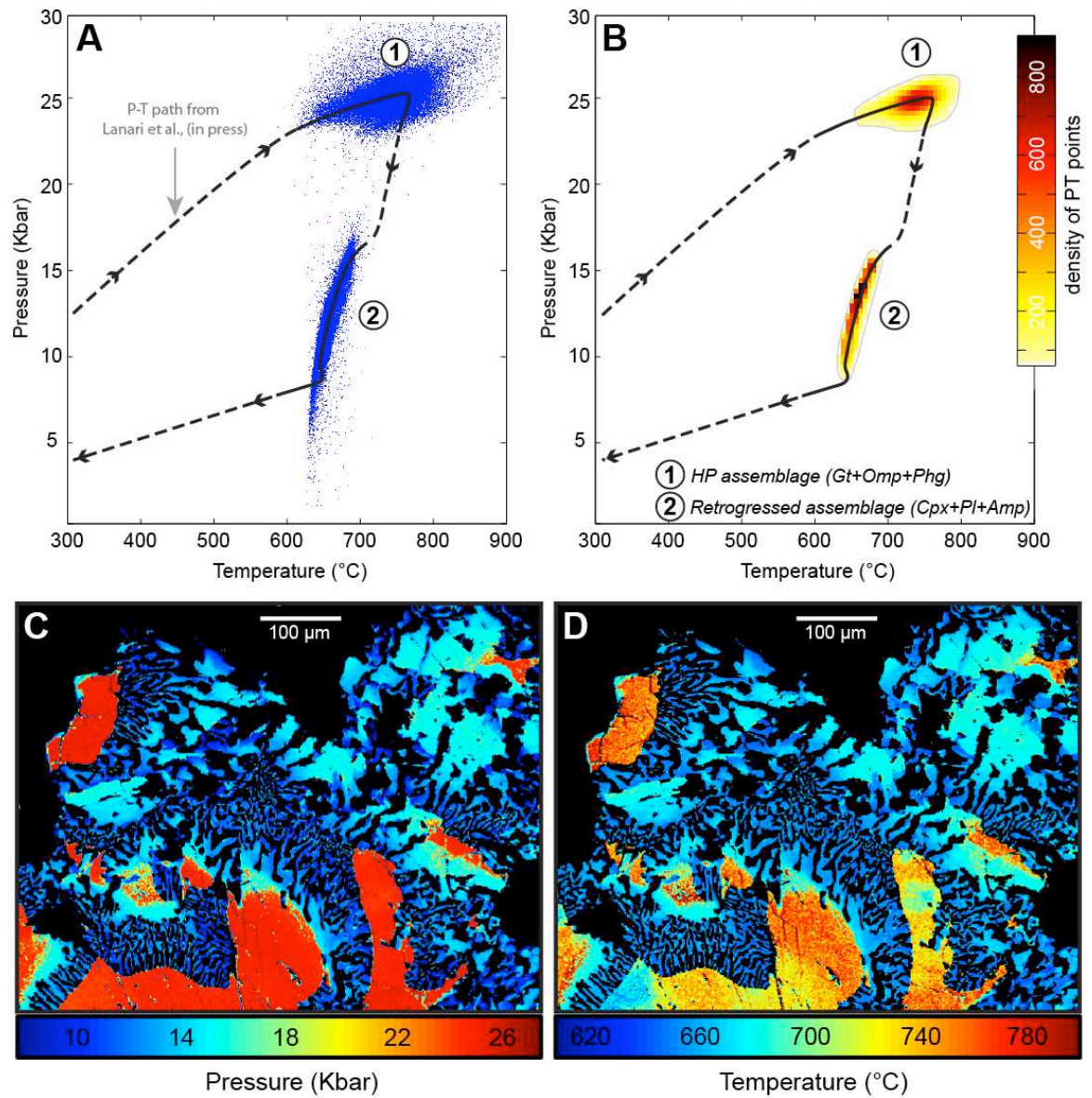
821

822

823

Figure 9

824



825

826

**Table 1**

<b>Group</b>	<b>Mineral (*)</b>	<b>End-members (**)</b>	<b>References</b>
<b>Chain silicates</b>	Amphibole (23)	<i>glaucophane (gl)</i> <i>tremolite (tr)</i> <i>f-tremolite (ftr)</i> <i>tschermakite (ts)</i> <i>pargasite (parg)</i> <i>cummingtonite (cum)</i> <i>ferri-tschermakite (mfets)</i>	Holland & Blundy, 1994; Dale et al. (2000, 2005); Spear (1995)
	Clinopyroxene (6)	<i>jadeite (jd)</i> <i>diopside (di)</i> <i>hedenbergite (hed)</i> <i>Ca-tschermak (cats)</i> <i>Acmite (acm)</i>	Spear (1995); Warren and Waters (2006)
	Orthopyroxene (6)	<i>Enstatite (en)</i> <i>Ferrosilite (fs)</i> <i>Mg-Tschermak (mgts)</i>	Holland and Powell (1998)
	Chloritoid (6)	<i>Fe-chloritoid (fctd)</i> <i>Mg-chloritoid (mctd)</i> <i>Mn-chloritoid (mnctd)</i>	Vidal et al. (1999)
	Staurolite (48)	<i>Fe-staurolite (fst)</i> <i>Mg-staurolite (mst)</i> <i>Mn-staurolite (mnst)</i>	Holland and Powell, (1998)
	Epidote (12.5)	<i>zoizite (zo)</i> <i>epidote (ep)</i> <i>Fe-epidote (fep)</i>	Holland and Powell, (1998)
	Cordierite (18)	<i>cordierite (crd)</i> <i>Fe-cordierite (fcrd)</i> <i>Mn-cordierite (mncrd)</i>	Holland and Powell, (1998)
<b>Ortho- &amp; ring silicates</b>	Garnet (12)	<i>almandine (alm)</i> <i>pyrope (pyr)</i> <i>spessartine (spe)</i> <i>grossular (gro)</i>	Spear (1995)
	Olivine (4)	<i>forsterite</i> <i>fayalite</i>	Spear (1995)
<b>Phyllosilicates</b>	Chlorite (14)	<i>amesite (ames)</i> <i>f-amesite (fames)</i> <i>daphnite (daph)</i> <i>sudoite (sud)</i> <i>chlorite-Mg (afchl)</i> <i>chlorite-Fe (fafchl)</i>	Holland et al. (1998); Vidal et al. (2001, 2005, 2006)
	Micas (11)	<i>celadonite (cel)</i> <i>f-celadonite (fcel)</i> <i>muscovite (mus)</i> <i>paragonite (par)</i> <i>margarite (marg)</i> <i>phlogopite (phl)</i> <i>f-phlogopite (fphl)</i> <i>pyrophyllite (prl)</i>	Coggon and Holland (2002); Parra et al. (2002); Dubacq et al. (2010)
<b>Framework silicates</b>	Feldspar (8)	<i>albite (ab)</i> <i>anortite (an)</i> <i>microcline (mic)</i>	Spear (1995)

828 \* Oxygen basis; \*\* abbreviation

830

**Table 2**

831

Method	Calibrations
Amphibole-Plagioclase	Blundy and Holland (1990); Holland and Blundy (1994)
Chlorite-Chloritoid	Vidal et al. (1999)
Garnet-Biotite	Thompson (1976); Goldman and Albee (1977); Holdaway and Lee (1977)
Garnet-Muscovite	Green and Hellman (1982); Krogh and R��heim (1978)
Garnet-Chlorite	Dickenson and Hewitt (1986); Grambling (1990)
Garnet-Amphibole	Ravna (2000b); Perchuk et al. (1985); Graham and Powell (1984)
Garnet-Cpx	Ravna (2000a); Ai (1994); Sengupta et al. (1989); Pattison and Newton (1989); Krogh (1988); Powell (1985); Dahl (1980); Ganguly (1979); Ellis and Green (1979); Mori and Green (1978); R��heim and Green (1974); Mysen and Heier (1972)

832

833

834

835

Table 3

836

Mineral	Thermometers	Barometers	Multi-equilibrium
<b>Amphibole</b>	T; Holland and Blundy (1994)	P; Anderson and Smith (1995) P; Schmidt (1992) P; Johnson and Rutherford (1989) P <sub>min</sub> ; Johnson and Rutherford (1989) P <sub>max</sub> ; Johnson and Rutherford (1989) P; Hollister et al. (1987) P; Hammarstrom and Zen (1986)	<b>Amphibole + plagioclase*</b> P from Schmidt (1992) and T from Holland and Blundy (1994). <b>Amphibole + plagioclase* + quartz*</b> P from Schmidt (1992) and T from Holland and Blundy (1994).
<b>Chlorite</b>	T; Inoue et al. (2009) T; Zang and Fyfe (1995) T; Jowett (1991) T; Hillier and Velde (1991) T; Cathelineau (1988) T; Kranidiotis and MacClean (1987) T; Cathelineau and Nieva (1985)		
<b>Clinopyroxene</b>		P; Waters (2002, 2003)	<b>Cpx + garnet* + phengite*</b> P from garnet – omphacite – phengites barometer of Waters and Martin (1993) and Waters (1996) and T from garnet – omphacite thermometer of Ravna (2000a) or Ellis and Green (1979). <b>Cpx + amphibole* + plagioclase*</b> T from amphibole – plagioclase thermometer of Holland and Blundy (1994) and P for the cpx – plagioclase barometer of Waters, (2002, 2003)
<b>K-White mica</b>		P; Massone and Schreyer (1987)	
<b>Garnet</b>	T; Creighton (2009) T; Kawasaki and Motoyoshi, (2011)		
<b>Rutile</b>	T; Zack et al. (2004)		

837

\* Fixed composition

838

839

840

841



842

**Table 4**

843

	Normalized	Classical	Difference (%)
Ti-oxide	0.43	0.43	0
Garnet	7.00	7.70	9.09
Fe-Oxide	1.10	1.13	2.65
Amphibole	13.20	12.77	3.37
Plagioclase	21.26	21.52	1.21
Omphacite	30.97	29.88	3.65
Cpx	26.04	26.57	1.99

844

845

846

**Table 5**

847

<b>Raw data</b>			<b>Quantified data</b>		
Element	Mean Intensity	Precision (% at $2\sigma$ )	Oxide	Composition	Error ( $2\sigma$ )
Si	11086	0.950	SiO <sub>2</sub>	54.718	0.528
Ti	93	10.35	TiO <sub>2</sub>	0.180	0.018
Al	2529	1.988	Al <sub>2</sub> O <sub>3</sub>	9.690	0.194
Fe	631	3.981	FeO	4.529	0.176
Mg	1381	2.689	MgO	10.211	0.276
Ca	6486	1.242	CaO	16.379	0.206
Na	470	4.609	Na <sub>2</sub> O	4.050	0.188
K	127	8.889	K <sub>2</sub> O	0.020	0.002
			<b>Structural formula</b>		
				Composition	Error ( $2\sigma$ )
			Si_T1	1.962	0.010
			Al_T1	0.038	0.010
			Al_M1	0.371	0.010
			Mg_M1	0.546	0.014
			Fe_M1	0.136	0.005
			Ca_M2	0.629	0.008
			Na_M2	0.281	0.013
			XMg	0.801	0.008
			XFe	0.199	0.008
			Xjd	0.281	0.013
			Xdi	0.546	0.014
			Xhed	0.136	0.005
			Xcats	0.019	0.005

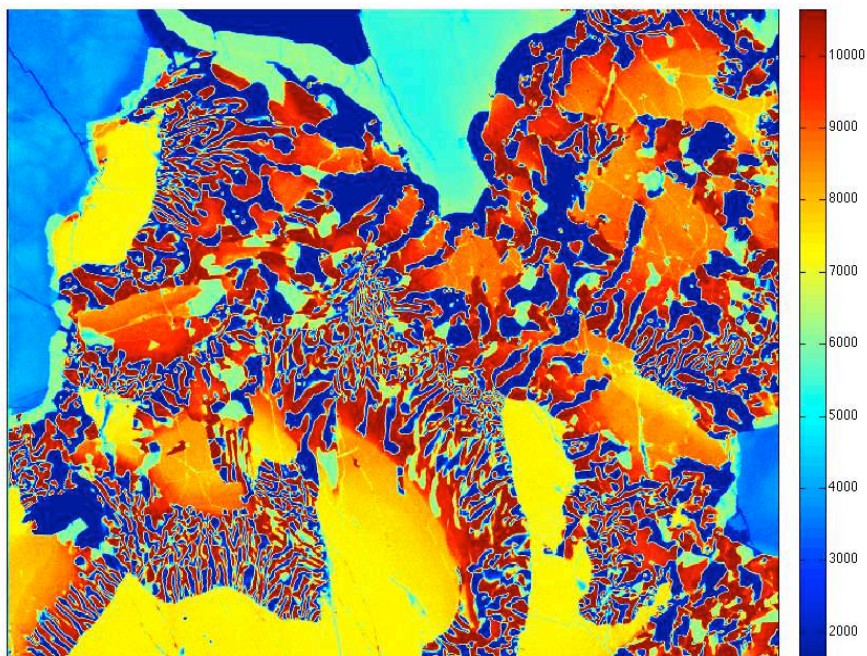
848

849

850

851 **Appendix 1**

852 Ca.txt (file)



853

854 *Ca.txt chemical image for the high-pressure Himalayan eclogite sample from the Stak*  
855 *massif in northern Pakistan displayed using XMapTools (unit number of recorded*  
856 *counts, auto-contrast).*

857

858

859

860